

Ultrabright γ-ray emission from the interaction of an intense laser pulse with a near-critical-density plasma

Aynisa Tursun(阿依妮萨·图尔荪), Mamat Ali Bake(买买提艾力·巴克), Baisong Xie(谢柏松), Yasheng Niyazi(亚生·尼亚孜), and Abuduresuli Abudurexiti(阿不都热苏力·阿不都热西提)

Citation: Chin. Phys. B, 2021, 30 (**11**): 115202. DOI: 10.1088/1674-1056/abfb59
Journal homepage: http://cpb.iphy.ac.cn; http://iopscience.iop.org/cpb

What follows is a list of articles you may be interested in

Multibeam Raman amplification of a finite-duration seed in a short distance

Y G Chen(陈雨谷), Y Chen(陈勇), S X Xie(谢善秀), N Peng(彭娜), J Q Yu(余金清), and C Z Xiao(肖成卓)
Chin. Phys. B, 2021, 30 (**10**): 105202. DOI: 10.1088/1674-1056/ac0521

Nonlinear propagation of an intense Laguerre-Gaussian laser pulse in a plasma channel

Mingping Liu(刘明萍), Zhen Zhang(张震), and Suhui Deng(邓素辉)
Chin. Phys. B, 2021, 30 (**5**): 055204. DOI: 10.1088/1674-1056/abd68c

Measurement of electronegativity during the E to H mode transition in a radio frequency inductively coupled Ar/O_2 plasma

Peng-Cheng Du(杜鹏程), Fei Gao(高飞, Xiao-Kun Wang(王晓坤), Yong-Xin Liu(刘永新), and You-Nian Wang(王友年)
Chin. Phys. B, 2021, 30 (**3**): 035202. DOI: 10.1088/1674-1056/abccb0

Propagation dynamics of relativistic electromagnetic solitary wave as well as modulational instability in plasmas

Rong-An Tang(唐荣安), Tiao-Fang Liu(刘调芳), Xue-Ren Hong(洪学仁), Ji-Ming Gao(高吉明), Rui-Jin Cheng(程瑞锦), You-Lian Zheng(郑有莲), and Ju-Kui Xue(薛具奎)
Chin. Phys. B, 2021, 30 (**1**): 015201. DOI: 10.1088/1674-1056/abb224

Suppression of auto-resonant stimulated Brillouin scattering in supersonic flowing plasmas by different forms of incident lasers

S S Ban(班帅帅), Q Wang(王清), Z J Liu(刘占军), C Y Zheng(郑春阳), X T He(贺贤土)
Chin. Phys. B, 2020, 29 (**9**): 095202. DOI: 10.1088/1674-1056/ab9c12

Ultrabright γ-ray emission from the interaction of an intense laser pulse with a near-critical-density plasma*

Aynisa Tursun(阿依妮萨·图尔荪)[1], Mamat Ali Bake(买买提艾力·巴克)[1,†], Baisong Xie(谢柏松)[2,‡], Yasheng Niyazi(亚生·尼亚孜)[3], and Abuduresuli Abudurexiti(阿不都热苏力·阿不都热西提)[1]

[1] *School of Physics Science and Technology, Xinjiang University, Urumqi* 830046, *China*

[2] *Key Laboratory of Beam Technology of the Ministry of Education, and College of Nuclear Science and Technology, Beijing Normal University, Beijing* 100875, *China*

[3] *Institute of Physics and Electrical Engineering, Kashi University, Kashgar* 844009, *China*

(Received 17 January 2021; revised manuscript received 20 April 2021; accepted manuscript online 26 April 2021)

An efficient scheme for generating ultrabright γ-rays from the interaction of an intense laser pulse with a near-critical-density plasma is studied by using the two-dimensional particle-in-cell simulation including quantum electrodynamic effects. We investigate the effects of target shape on γ-ray generation efficiency using three configurations of the solid foils attached behind the near-critical-density plasma: a flat foil without a channel (target 1), a flat foil with a channel (target 2), and a convex foil with a channel (target 3). When an intense laser propagates in a near-critical-density plasma, a large number of electrons are trapped and accelerated to GeV energy, and emit γ-rays via nonlinear betatron oscillation in the first stage. In the second stage, the accelerated electrons collide with the laser pulse reflected from the foil and emit high-energy, high-density γ-rays via nonlinear Compton scattering. The simulation results show that compared with the other two targets, target 3 affords better focusing of the laser field and electrons, which decreases the divergence angle of γ-photons. Consequently, denser and brighter γ-rays are emitted when target 3 is used. Specifically, a dense γ-ray pulse with a peak brightness of 4.6×10^{26} photons/s/mm^2/mrad^2/0.1%BW (at 100 MeV) and 1.8×10^{23} photons/s/mm^2/mrad^2/0.1%BW (at 2 GeV) are obtained at a laser intensity of 8.5×10^{22} W/cm^2 when the plasma density is equal to the critical plasma density n_c. In addition, for target 3, the effects of plasma channel length, foil curvature radius, laser polarization, and laser intensity on the γ-ray emission are discussed, and optimal values based on a series of simulations are proposed.

Keywords: electron acceleration, γ-ray emission, inverse Compton scattering, near-critical-density plasma, 2D-QED-PIC simulation

PACS: 52.38.–r, 52.38.ph, 52.65.–y **DOI:** 10.1088/1674-1056/abfb59

1. Introduction

Owing to the rapid development of laser technology,[1,2] ultra-intense (10^{22} W/cm^2) and ultrashort (a few femtoseconds) laser pulses can be obtained in the laboratory.[3] Laser intensities in the order of 10^{23}–10^{25} W/cm^2 are expected to become available in the next few years.[4,5] When an ultrahigh-intensity laser interacts with a plasma, the electron motion becomes relativistic,[6,7] and quantum electrodynamics (QED) effects such as γ-ray emission[8] and electron–positron pair production become significant.[9,10] Considerable theoretical and numerical[11–13] research on the generation of high-energy electrons and ultrabright γ-rays has been conducted for applications in medicine,[14] industry,[15] and astrophysics.[16] Many researchers have proposed various schemes for obtaining high-energy electron sources for γ-ray generation, such as laser-driven direct laser acceleration (DLA),[17,18] radiation pressure acceleration,[19] and laser wakefield acceleration (LWFA).[20,21] Among them, LWFA is the most widely studied and thought to be a more straightforward γ-ray emission mechanism, along with the all-optical mechanism.[22]

Recent studies have shown that electron beams with energies as high as several GeV can be obtained from laser–plasma interactions using LWFA,[23,24] and γ-photons with energies beyond the GeV regime can be produced by nonlinear Compton scattering as the wakefield-accelerated electron beam interacts with the reflected laser pulse.[25,26] Many researchers have studied effective mechanisms for producing γ-rays with a peak brilliance of 10^{20}–10^{26} photons/s/mm^2/mrad^2/0.1%BW at MeV to GeV energies using lasers with intensities of 10^{21}–10^{23} W/cm^2.[27,28] Zhu *et al.*[29] recently obtained γ-rays with a peak brilliance of 10^{26} photons/s/mm^2/mrad^2/0.1%BW at 1 MeV using a multi-petawatt laser pulse in a two-stage wakefield accelerator. Gu *et al.*[30] proposed a new mechanism for generating brilliant γ-rays using a plasma mirror and obtained γ-rays with a peak intensity of 0.74 PW and a brilliance of 10^{24} photons/s/mm^2/mrad^2/0.1%BW at 58 MeV under a laser intensity of 10^{23} W/cm^2. In a recent study, we investigated an efficient method of generating high-energy γ-photons using the interaction between a wakefield-accelerated electron beam and a counter-propagating high-intensity laser pulse with a

*Project supported by the National Natural Science Foundation of China (Grant Nos. 11664039, 11875007, and 11664040).

†Corresponding author. E-mail: mabake@xju.edu.cn

‡Corresponding author. E-mail: bsxie@bnu.edu.cn

© 2021 Chinese Physical Society and IOP Publishing Ltd

compound target, and obtained two groups of γ-rays with a small divergence angle.[31] Chang *et al.*[32] proposed a new resonance acceleration scheme for generating relativistic electron bunches and brilliant γ-rays, used a three-dimensional particle-in-cell (PIC) simulation and reported γ-ray pulses with a peak brilliance of 10^{25} photons/s/mm^2/mrad^2/0.1%BW (15 MeV) at a laser intensity of 1.9×10^{23} W/cm^2. More recently, Zhang *et al.*[33] reported nano-micro array thin target for ultra-short (440 as) and ultra-bright [10^{24} photons/s/mm^2/mrad^2/0.1%BW (15 MeV)] γ-ray emission with high conversion efficiency. These high-energy electrons and γ-rays represent a novel light source with a broad range of applications in the production of high-energy electron-positron pairs, exploring high-energy astrophysics in the laboratory, and performing nuclear physics research.[34,35]

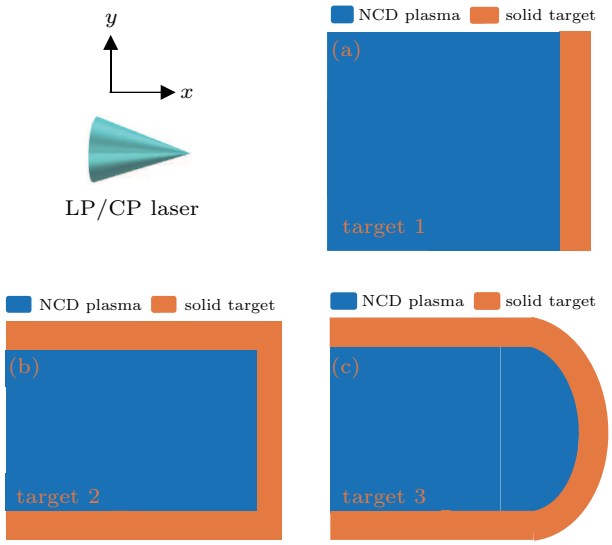


Fig. 1. Schematic diagram of ultrabright γ-ray emission from the interaction of an intense LP laser and a compound target. The targets consist of a uniform NCD hydrogen plasma with a density of $n_e = n_c$ and an aluminum solid foil with a density of $n_e = 700n_c$. Blue and orange represent the NCD plasma and solid target, respectively.

In this study, we investigate the generation of high-energy, ultrabright γ-rays by the interaction of an intense linearly polarized (LP) laser with a near-critical-density (NCD) plasma using two-dimensional (2D) QED PIC simulations. In the simulations, three target configurations are used to investigate the effects of target shape on γ-ray generation, as shown in Fig. 1. The γ-photon density, energy, angular distribution, and peak brightness for each target are compared in detail. The results show that when a laser pulse with an intensity of 8.5×10^{22} W/cm^2 propagates in an NCD plasma, a large amount of electrons are trapped by the self-generated magnetic field and radiation reaction (RR) trapping effects and accelerated to high energy. Consequently, γ-rays are emitted by nonlinear betatron oscillation in the first stage and by nonlinear Compton scattering in the second stage. The accelerated electrons emit GeV γ-photons by inverse Compton scattering when they collide with the reflected laser pulse. The simulation results indicate that target 3 affords better focusing of both the laser field and electron beam compared to targets 1 and 2. Consequently, well-collimated γ-rays with high energy, high density, and low divergence angle are produced when target 3 is used. The density and cutoff energy of both the accelerated electrons and the emitted γ-rays are much higher than those obtained by other proposed mechanisms[36,37] using the same driving laser. The angular distribution of the γ-rays is within approximately $\theta \leq 20^\circ$, and the cutoff energies of the accelerated electrons and γ-photons exceed 3 GeV and 2 GeV, respectively. The brilliance of the γ-rays and the conversion efficiency are higher than those reported in Ref. [38], where two counter-propagating intense laser pulses were used. The results demonstrate that it is essential to optimize the shape of the solid target to enhance the γ-ray energy and brilliance and the conversion efficiency.

2. Theoretical model of γ-ray emission

When an ultrahigh-intensity laser pulse interacts with a plasma, electrons are simultaneously affected by the RR force and emit high-energy γ-photons. When the laser intensity is relatively high, the RR force becomes non-negligible.[39] In laser–plasma interactions, the relativistic gauge-invariant parameter χ_e determines the importance of the nonlinear QED effects and the ratio of γ-ray emission.[40] In the classical description, the total radiation power of the accelerated electrons is written as[41]

$$P = \frac{e^2\gamma_e^2 \boldsymbol{F}^2}{6\pi\varepsilon_0 m_e^2 c^3}, \tag{1}$$

where $\boldsymbol{F} = \mathrm{d}\boldsymbol{P}/\mathrm{d}t$, $\boldsymbol{P}$ is the electron momentum, m_e and e are the mass and charge of the electron, respectively, c is the speed of light in vacuum, and γ_e is the electron Lorentz factor. The classical description of electron radiation in a strong electromagnetic field overestimates the total emitted power. In the quantum description, the emitted photon energy may not exceed the electron energy, whereas there is no such restriction in the classical description. We introduce the quantum effect function $G(\chi_e)$, which decreases the electron radiation power,[43] into the classical expression. The quantum effects can be expressed as[42]

$$P_{\mathrm{Rad}} = -\frac{2}{3}a_f\frac{m_e^2c^4}{\hbar}\chi_e^2 G(\chi_e), \tag{2}$$

where $a_f = e^2/\hbar c$ is the fine-structure constant, $\hbar$ is the Planck constant, and $G(\chi_e) \approx (1 + 18\chi_e + 69\chi_e^2 + 73\chi_e^3 + 8.506\chi_e^4)^{-1/3}$.[43] By comparing Eqs. (1) and (2), we obtain

$$\chi_e^2 = \frac{\hbar^2 e^2 \gamma_e^2}{4c^2 m_e^4 \pi\varepsilon_0}\left|\frac{\mathrm{d}\boldsymbol{P}}{\mathrm{d}t}\right|^2, \tag{3}$$

where $\left|\frac{\mathrm{d}\boldsymbol{P}}{\mathrm{d}t}\right|^2 = \left|m_\mathrm{e}(\gamma_\mathrm{e}\frac{\mathrm{d}\boldsymbol{v}}{\mathrm{d}t} + \boldsymbol{v}\frac{\mathrm{d}\gamma_\mathrm{e})}{\mathrm{d}t}\right|^2$. Substituting this expression in Eq. (3), we obtain the relativistic gauge-invariant parameter

$$\chi_\mathrm{e} = \frac{\gamma_\mathrm{e}}{E_\mathrm{s}}\sqrt{(\boldsymbol{E}+\frac{1}{c}\boldsymbol{v}\times\boldsymbol{B})^2 - \frac{1}{c^2}(\boldsymbol{v}\cdot\boldsymbol{E})^2}, \tag{4}$$

where $\boldsymbol{v}$ is the electron velocity, $E_\mathrm{s} = a_\mathrm{f} e/r_\mathrm{e}^2$ is the Schwinger critical field, $r_\mathrm{e} = e^2/(m_\mathrm{e}c^2)$ is the classical electron radius, and $\boldsymbol{E}$ and $\boldsymbol{B}$ are the laser electric and magnetic fields, respectively. Under ultrarelativistic conditions ($\chi_\mathrm{e} \geq 1$), when the accelerated electron beam interacts with the reflected laser pulse, the electron velocity decreases, and thus the Lorentz factor of the electrons increases. Consequently, the photon emission probability is maximized $\chi_\mathrm{e}^{\uparrow\downarrow} \simeq 2\gamma_\mathrm{e}(E/E_\mathrm{s})$. However, in the co-propagating case, it decreases dramatically to $\chi_\mathrm{e}^{\uparrow\uparrow} \simeq (2\gamma_\mathrm{e})^{-1}(E/E_\mathrm{s})$.

3. Simulation setups

To test our model, a 2D-PIC simulation was conducted using the EPOCH code,[44] which takes into account of the QED effects via a Monte Carlo algorithm. In our simulation, the simulation box has dimensions of (110×24) μm in the x and y directions, respectively, and is divided into 3300×400 grid cells, with 10 macroparticles in each cell. An LP Gaussian laser pulse with an intensity of $I_0 = 8.5\times 10^{22}$ W/cm^2 enters the simulation box from the left boundary at $t = 0$. The corresponding normalized amplitude is $a_0 = eE_0/m_\mathrm{e}c\omega_0 = 250$, where E_0 and ω_0 are the laser electric field strength and laser frequency, respectively. The laser pulse duration is $\tau = 15$ fs, the laser wavelength is $\lambda_0 = 1$ μm, and the spot size of the laser is $r_0 = 5$ μm in all the simulations. Three target configurations are considered, as shown in Fig. 1. For target 1, a flat foil with no channel is attached behind the NCD plasma, as shown in Fig. 1(a). Flat and curved foils with an NCD plasma channel are used as targets 2 and 3, as shown in Figs. 1(b) and 1(c), respectively. The NCD plasma is a uniform hydrogen plasma with a density $n_\mathrm{e} = n_\mathrm{c}$, and solid aluminum foils with a density $n_\mathrm{e} = 700n_\mathrm{c}$ are used, where n_e is the electron density, and $n_\mathrm{c} = m_\mathrm{e}\omega_0^2/4\pi e^2$ is the critical density. The NCD plasma is located between $x = 10$ μm and $x = 100$ μm, and between $y = -6$ μm and $y = 6$ μm, and the thickness of the aluminum foil is 2 μm. Simple outflow and periodic boundary conditions are applied in the x and y directions, respectively.

4. Simulation results

When an intense laser propagates in an NCD plasma, electrons and ions are separated by the strong laser ponderomotive force in both the longitudinal and transverse directions. A large number of electrons are trapped in the laser field owing to the RR trapping effect (as discussed in Subsection 5.5), which results in an electron current in the opposite direction in the plasma channel and produces a self-generated magnetic field. The distribution of the self-generated magnetic field for each target before ($t = 350$ fs) and after ($t = 360$ fs) laser reflection are plotted in Fig. 2. A low-intensity magnetic field with large divergence is formed when target 1 is used, as shown in Figs. 2(a) and 2(b). However, when targets 2 and 3 are used, the magnetic field is stronger and is focused more tightly, and it maintains its shape well for a relatively long spatial distance, as shown in Figs. 2(c)–2(f). When the self-generated magnetic field is strong enough to pinch and trap expelled electrons, an overdense electron bunch is formed in the center of the NCD plasma channel, as shown in Fig. 3. This result indicates that the plasma channel plays a significant role in the generation of a transverse focusing magnetic field, which can effectively suppress the electron beam divergence in the transverse direction. In our scheme, the NCD plasma density is $n_\mathrm{e} = n_\mathrm{c}$, and the effective critical density is $n_\mathrm{eff} = n_\mathrm{c}\sqrt{1+a_0^2/2} \approx 177n_\mathrm{c}$ for a laser intensity of $a_0 = 250$. Therefore, the plasma is completely transparent to the incident laser pulse, and the electron acceleration in the plasma channel is very similar to wakefield acceleration, but not to DLA acceleration, as shown in Fig. 3. This behavior ultimately enhances the probability of γ-ray emission.

Figure 3 shows the density distributions of electrons and photons for each target after laser reflection ($t = 360$ fs). Under the same laser and NCD plasma conditions, the electron and photon density profiles for targets 2 and 3 are completely different from that for target 1. For target 1, because of inefficient focusing by the self-generated magnetic field, a large number of electrons escape the channel center, and thus the electron beam has a large source size, as shown in Fig. 3(a). Consequently, γ-rays with low density and a large source size are produced, as shown in Fig. 3(b). However, for targets 2 and 3, because the self-generated magnetic field affords better focusing, electrons are confined in a small space on the laser propagation axis and produce high-density γ-rays with a density distribution similar to that of the electrons, as shown in Figs. 3(d) and 3(f). The photon density was approximately $90n_\mathrm{c}$ and $120n_\mathrm{c}$ for targets 2 and 3, which are three and four times higher, respectively, than the value of approximately $30n_\mathrm{c}$ for target 1. The results indicate that up and down solid foils (the channel) plays an important role in focusing the laser and generating a magnetic field, which is favorable for obtaining a low-divergence, high-density electron beam and γ-rays. Note that more tightly focused and denser γ-photons are generated when target 3 is used than when target 2 is used. The reason is that target 3 provides better focusing of the laser field as well as the electrons.

Figure 4 shows the energy spectra of electrons and γ-

photons for each target configuration at $t = 300$ and 360 fs (before and after laser reflection, respectively). In the first stage of the interaction, an intense laser propagates in the NCD plasma. Because of the additional contributions of the self-generated magnetic field and RR trapping effect, a large number of electrons are trapped and accelerated to high energy. The cutoff energy of the accelerated electrons at $t = 300$ fs is 3 GeV for target 3 but only approximately 1.5 GeV for target 1, as shown in Fig. 4(a). Consequently, some low-energy γ-photons are emitted via nonlinear betatron oscillation when target 1 is used, as shown in Fig. 4(b). However, the γ-photon cutoff energies for targets 2 and 3 are much higher than that for target 1. This result also indicates that the NCD plasma channel plays a key role in the generation of high-energy γ-rays. In the second stage, the accelerated electrons collide with the counter-propagating reflected laser, and the strong ponderomotive force of the laser changes the electron direction and thus increases the electron Lorentz factor γ_e. Therefore, the value of the quantum invariant parameter χ_e is maximized, increasing the probability of γ-ray emission and the γ-ray energy. In this stage, because nonlinear Compton scattering occurs, the energy of some of the accelerated electrons is decreased, and high-energy γ-photons are emitted, as shown in Fig. 4(d). Note that, for target 3, the cutoff energy of γ-photons is 2.2 GeV, whereas it is only approximately 500 MeV for target 1.

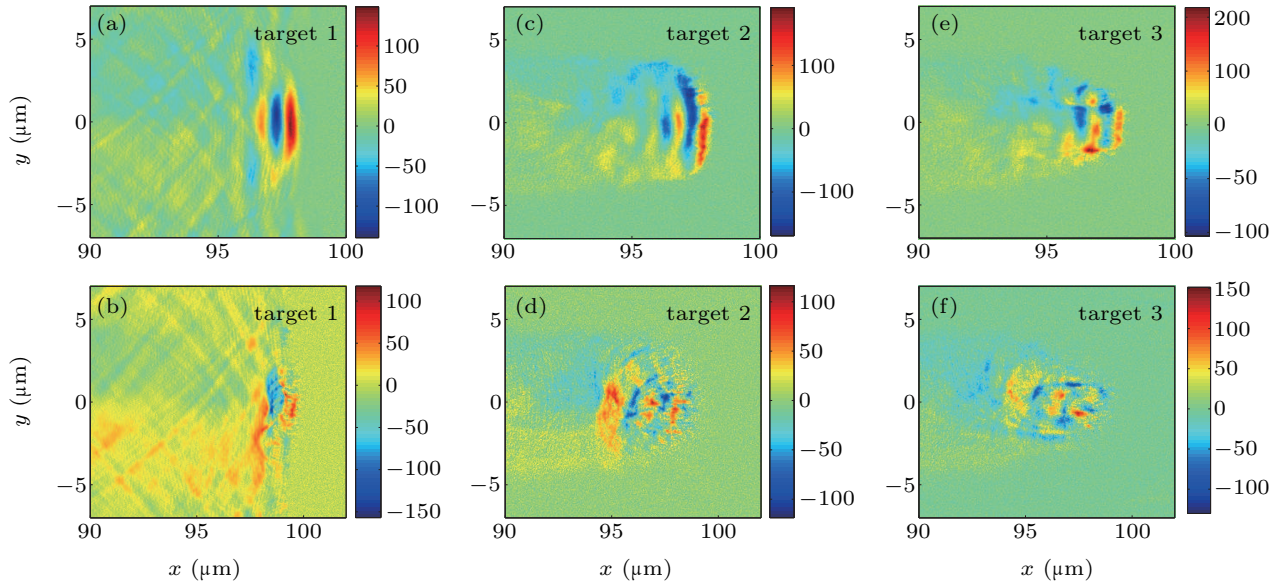


Fig. 2. Distribution of self-generated magnetic field $\boldsymbol{B}_z$ in (x, y) plane for three targets before ($t = 350$ fs, top row) and after ($t = 360$ fs, bottom row) laser reflection. The magnetic field is normalized by $B_0 = m_e\omega_0/e$.

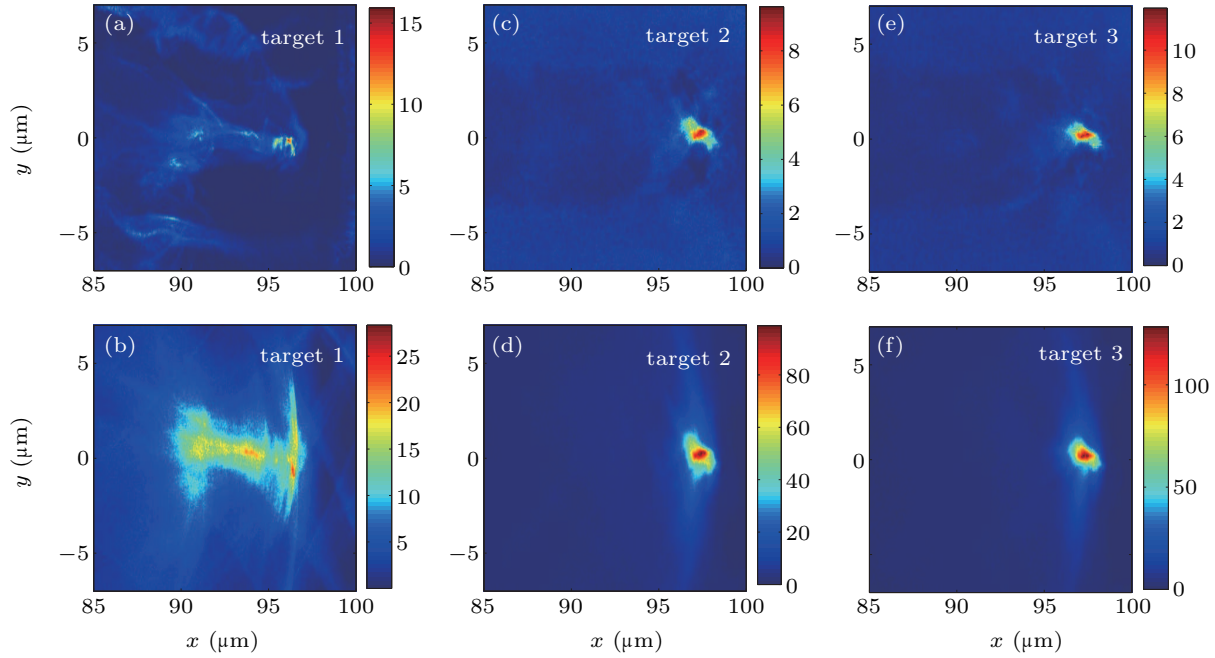


Fig. 3. Distribution of electron (top row) and photon (bottom row) densities in (x, y) plane for each target after laser reflection ($t = 360$ fs). The electron and photon densities are normalized by the critical density n_c.

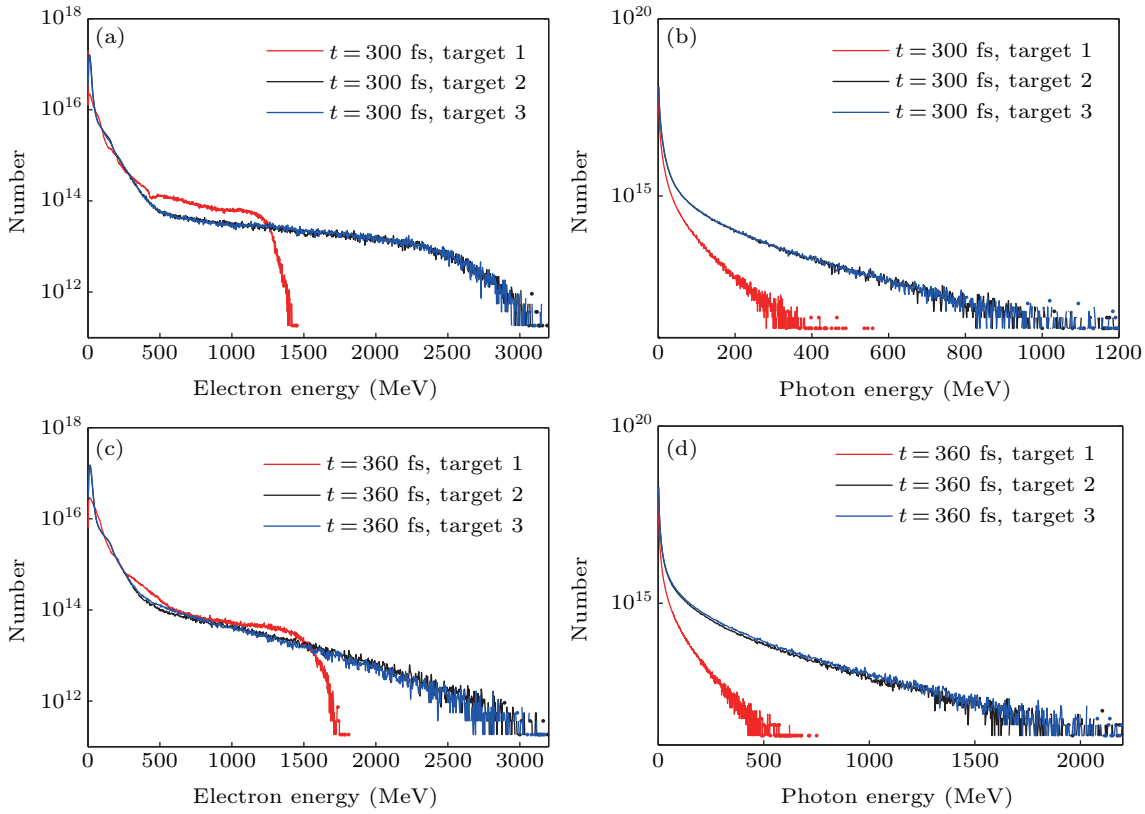


Fig. 4. Energy spectra of electrons [(a) and (c)] and γ-photons [(b) and (d)] for each target before (top row) and after (bottom row) laser reflection.

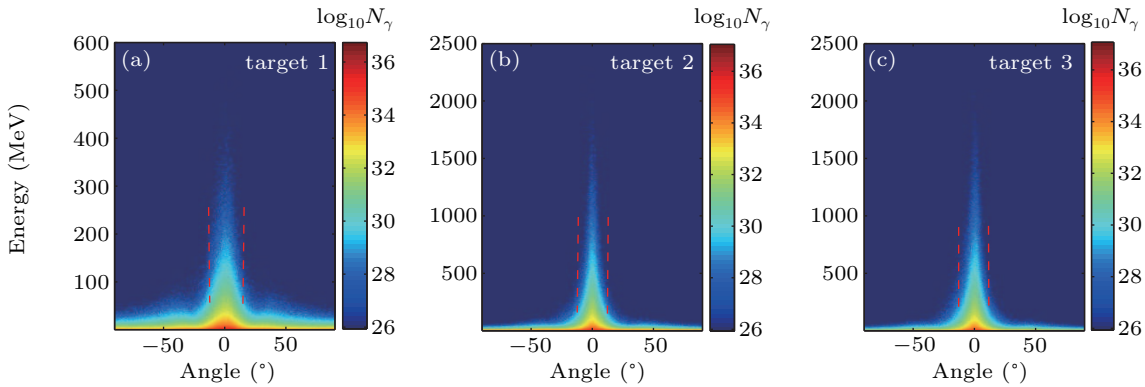


Fig. 5. Energy angular distribution of γ-photons for each target after laser reflection ($t = 360$ fs). The color bar shows the photon number (N_γ) on a logarithmic ($\log_{10} N_\gamma$) scale with arbitrary units.

Table 1. γ-ray peak brilliance $B(k)$ (photons/s/mm^2/mrad^2/0.1%BW) for each target at $t = 360$ fs.

Energy (MeV)	Target 1		Target 2		Target 3	
	Photon number	$B(k)$	Photon number	$B(k)$	Photon number	$B(k)$
100	2×10^{14}	1×10^{24}	1.84×10^{15}	1.6×10^{26}	1.84×10^{15}	4.6×10^{26}
500	3.67×10^{11}	2×10^{21}	5×10^{14}	5.3×10^{25}	5×10^{14}	1.2×10^{26}
1000	–	–	8.25×10^{13}	8.7×10^{24}	8.25×10^{13}	2.1×10^{25}
1500	–	–	8.57×10^{12}	9×10^{23}	8.57×10^{12}	2×10^{24}
2000	–	–	7.33×10^{11}	7.7×10^{22}	7.33×10^{11}	1.8×10^{23}

Figure 5 plots the energy angular distribution of γ-photons for each target configuration after laser reflection ($t = 360$ fs). Low-energy γ-photons with a large divergence angle ($\sim 37°$) are generated when target 1 is used, as shown in Fig. 5(a). However, for targets 2 and 3, the divergence angles of the γ-photons are approximately 25.5° and 20.5°, as shown in Figs. 5(b) and 5(c), respectively. The corresponding γ-ray peak brilliance for each target at $t = 360$ fs is given in Table 1. It can be concluded that, for target 1, there are 2×10^{14} and 3.67×10^{11} photons at 100 MeV and 500 MeV, respectively, within a source size of 7.2×4 μm^2, which gives a peak brightness

of approximately 1×10^{24} photons/s/mm^2/mrad^2/0.1%BW at 100 MeV and 2×10^{21} photons/s/mm^2/mrad^2/0.1%BW at 500 MeV. By contrast, for target 2, the peak brightness of the γ-rays at 100 MeV (source size is 1.63×2.05 μm^2) is 1.6×10^{26} photons/s/mm^2/mrad^2/0.1%BW, and for target 3, it is 4.6×10^{26} photons/s/mm^2/mrad^2/0.1%BW (source size is 1.37×1.45 μm^2), which is two orders of magnitude larger than that for target 1. The well-collimated, high-density, and ultrabright γ-rays obtained using our scheme may be suitable for the generation of energetic positrons and for laboratory astrophysics research.

5. Discussion

The fraction of energy coupled to electrons and the relaxation time are related to the laser and plasma parameters, as discussed in previous papers.[45–47] Therefore, in this section, we discuss in detail the effects of plasma channel length, target curvature radius, laser polarization, laser intensity, and the RR force on the electron acceleration and γ-ray emission.

5.1. Effect of plasma channel length

We study the effects of NCD plasma channel length on the electron acceleration and γ-ray emission for target 3 with a fixed target curvature radius of $r = 6$ μm. To ensure that the laser is reflected from the foil and collides with the accelerated electrons, we consider the following times and channel lengths: $t = 300$ fs for $L = 80$ μm, $t = 330$ fs for $L = 90$ μm, $t = 360$ fs for $L = 100$ μm, $t = 390$ fs for $L = 110$ μm, and $t = 420$ fs for $L = 120$ μm. The simulation results show that for short channels, for example, $L = 80$ μm and $L = 90$ μm, trapped electrons are accelerated to lower energies because of the short acceleration distance, and thus lower-energy electrons and γ-photons are produced, as shown in Figs. 6(a) and 6(b). However, for long channels, for example, $L = 110$ μm and $L = 120$ μm, the travel time is longer, and most of the laser energy is depleted before laser reflection (the laser energy after reflection is approximately 100 J, which is one-tenth the initial laser energy). Under these conditions, the photons also have lower energies than those produced at $L = 100$ μm. As shown in Fig. 9(b), the electron energy conversion efficiency increased linearly until $t = 300$ fs, remained constant for 60 fs, and then decreased. This result indicates that a long channel (i.e., a long travel time) is not favorable for electron acceleration. When a channel length of $L = 100$ μm is used, the accelerated electron cutoff energy is as high as 3 GeV, and the corresponding γ-photon energy exceeds that obtained using the other channel lengths. Figures 6(c) and 6(d) show that the peak brightness of γ-photons and the conversion efficiency of laser energy to electrons and γ-photons are higher than those at the other channel lengths. This result shows that to obtain high-energy γ-rays, it is very important to choose an appropriate channel length.

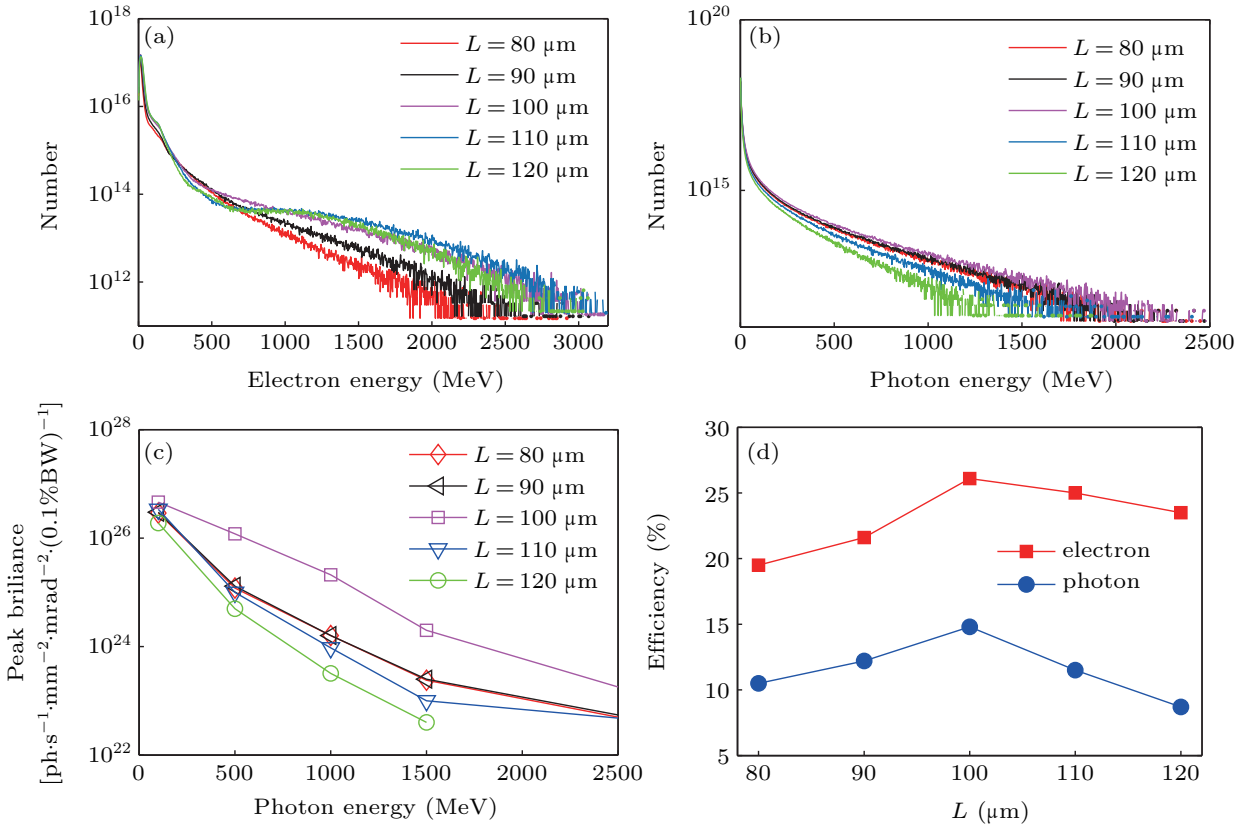


Fig. 6. Energy spectra of (a) electrons and (b) γ-photons, (c) γ-ray peak brilliance (photons/s/mm^2/mrad^2/0.1%BW), and (d) energy conversion efficiency of electrons and γ-photons for different plasma channel lengths.

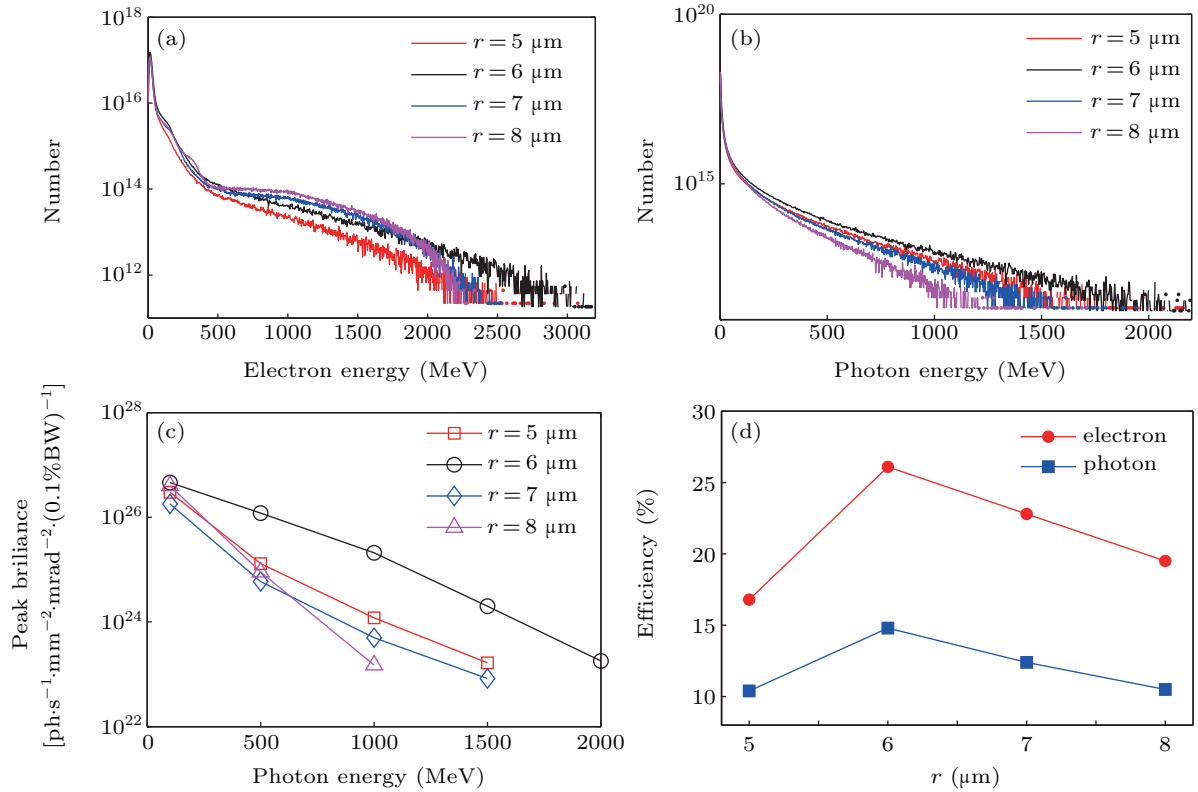


Fig. 7. Energy spectra of (a) electrons and (b) γ-photons, (c) γ-ray peak brilliance (photons/s/mm^2/mrad^2/0.1%BW), and (d) energy conversion efficiency of electrons and γ-photons for different target curvature radii after laser reflection ($t = 360$ fs).

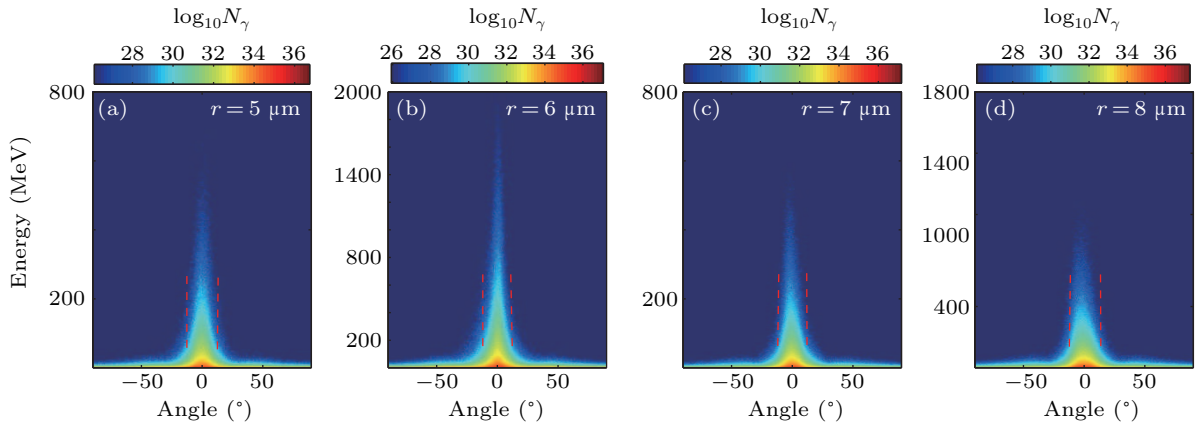


Fig. 8. Energy angular distribution of γ-photons for different foil curvature radii after laser reflection ($t = 360$ fs). The color bar shows the photon number (N_γ) on a logarithmic ($\log_{10}N_\gamma$) scale with arbitrary units.

5.2. Effect of target curvature radius

The effects of target curvature radius on the electron acceleration and γ-ray emission are also investigated for target 3 with a fixed channel length of $L = 100$ μm. The simulation results show that when the radius of curvature of the target is equal to or smaller than the laser spot size, $r_0 = 5$ μm, the number of trapped electrons is limited; thus, a relatively small number of electrons interact with the reflected laser, and thus the electron and photon energies are low, as shown in Figs. 7(a) and 7(b). Figures 7(c) and 7(d) show that the peak brightness of the γ-rays and the energy conversion efficiency decrease with increasing curvature radius. The primary reason is that the laser field is less focused at a relatively large curvature radius, which results in a large γ-ray divergence. In addition, the divergence angle of γ-photons is also relatively wide at a small curvature radius, as shown in Fig. 8(a). At $r = 6$ μm, more electrons are trapped in the channel and they are accelerated to higher energy than in the other cases. Consequently, γ-photons with higher energy and a smaller divergence angle are emitted. For this optimal radius, the electron and photon cutoff energies are 3 GeV and 2.2 GeV, respectively, and the divergence angle of the γ-rays is approximately 20.5°, as shown in Fig. 8(b). The results show that the maximum electron and photon energies both decrease significantly with increasing radius of curvature. From these simulation results,

we can conclude that large and small curvature radii decrease the focusing of the laser field and the trapping of electrons in the channel, and ultimately decrease the maximum energy and increase the γ-ray divergences angle. For both simulations and experiments, it is crucial to select a target with an appropriate curvature radius to generate high-quality γ-rays.

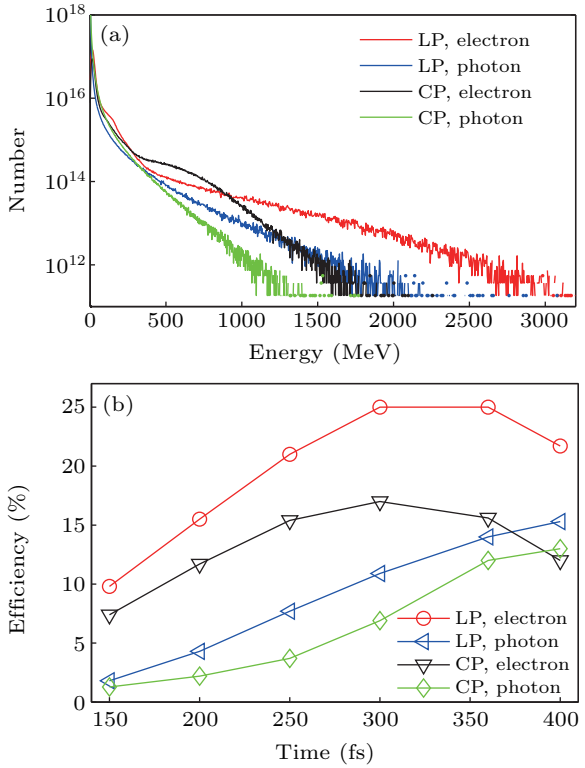


Fig. 9. Energy spectra of (a) electrons and γ-photons for LP and CP lasers at $t = 360$ fs, (b) time evolution of energy conversion efficiency for LP and CP lasers at $t = 360$ fs.

5.3. Effect of laser polarization

It is well-known that in laser–plasma interaction, the laser polarization is an important factor that affects the electron acceleration and the production of high-energy, ultrabright γ-rays. In this subsection, we describe an additional simulation that was performed to investigate the effects of laser polarization on γ-ray emission by using LP and circularly polarized (CP) laser pulses with the same laser energy and optimal plasma parameters. Figure 9(a) shows that when the LP laser is used, both the accelerated electrons and γ-photons have much higher energies than when the CP laser is used. The reason is that for the LP laser, the ponderomotive force is $\boldsymbol{F}_{\mathrm{LP}} = -\left(e^2/8m_{\mathrm{e}}\omega_0^2\right)\Delta E_0^2(x)[1-\cos(2\omega_0 x)]$.[46] The oscillation component of the ponderomotive force causes additional electron heating compared to that for the CP laser. More importantly, the heated electrons are captured in the center by the combined effects of RR trapping and the self-generated magnetic field, as shown in Fig. 11. Consequently, more electrons collide with the reflected laser in the second stage, and they emit more high-energy γ-photons, as shown in Fig. 9(a). The time evolution of the energy conversion efficiencies from laser to electrons and γ-photons are presented in Fig. 9(b). We also summarized our results in Table 2, it shows that the energy conversion efficiencies of electrons and γ-photons are approximately 26% and 15% for the LP laser, respectively, but they are only approximately 15% and 12% for the CP laser. We see that there is a significant difference between the LP and CP lasers.

5.4. Effect of laser intensity

It is essential to investigate the effect of laser intensity on ultrabright γ-ray emission from laser–plasma interaction. Using another simulation, we investigated the effect of laser intensity using the optimal laser (the LP laser) and plasma parameters and the results are summarized in the Table 2. The simulation results show that the electron and γ-ray energies increase with increasing laser intensity a_0, as shown in Figs. 10(a) and 10(b). The reason is that the higher laser intensity produces more energetic electrons owing to the combined effects of the stronger acceleration field, self-generated magnetic field, and RR trapping effect, ultimately strengthening the emission of well-collimated γ-rays, as shown in Fig. 10(c). Figure 10(d) shows the energy conversion efficiencies of electrons and γ-photons as a function of laser amplitude a_0 for the optimal laser and plasma parameters. The energy conversion efficiency of electrons increased linearly up to $a_0 = 150$ and then increased more steeply with a_0. The conversion efficiency to photons increased rapidly from a few percent to 26%, and the conversion efficiencies of electrons and γ-photons were comparable at approximately $a_0 = 300$ (see Table 2). As the laser intensity increased, photons absorbed more energy than electrons, as shown in Fig. 10(d).

5.5. Effect of radiation reaction

For comparison, we also performed additional simulations without the RR effect using the optimal target parameters for the LP laser and the results are also summarized in the Table 2. The simulation results indicated that without the RR trapping effect, the strong ponderomotive force of the intense laser tends to push electrons from the high-intensity region. Consequently, few electrons are trapped in the channel center, and they diverge in the transverse direction at the acceleration stage, as shown in Figs. 11(a) and 11(b). However, when the RR effect is considered, the electrons in the NCD plasma experience a strong RR force due to radiating photons. When the RR force becomes large enough to compensate for the expelling ponderomotive force of the laser, the RR causes electrons to be trapped inside the laser instead of removed by ponderomotive pressure.[48] Consequently, electrons gradually accumulate in the high-intensity region (channel center) and

form a high-density electron bunch, as shown in Figs. 11(a1) and 11(b1). This electron bunch then co-propagates with the laser pulse and is accelerated to high energy in the first stage; thus, it emits more high-energy, well-collimated γ-photons in the first stage, as shown in Figs. 11(c1) and 11(d1). We see from this figure that the photon density exceeds $50n_c$ when the RR is considered, which is much higher than that without the RR, as shown in Figs. 11(c) and 11(d). In the second stage of the interaction, this well-collimated electron beam counter-propagates with the reflected laser pulse, and the γ-ray emission is enhanced by inverse Compton scattering, as discussed in Section 4.

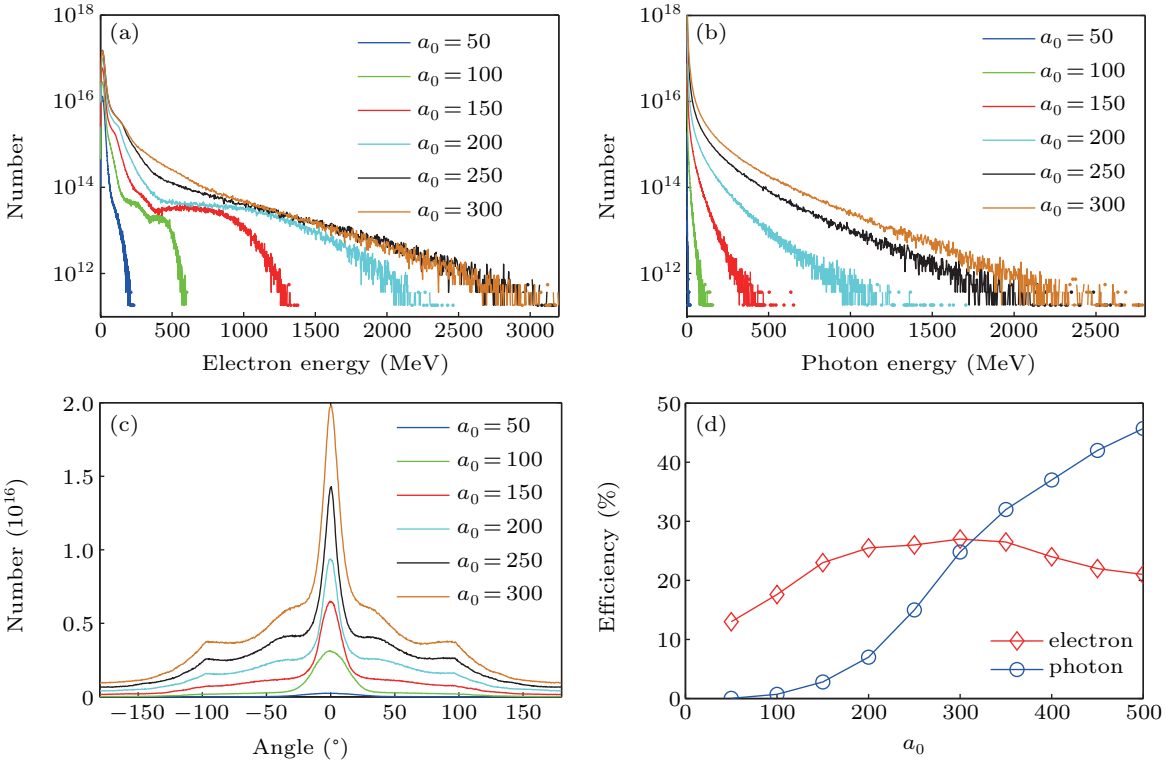


Fig. 10. Energy spectra of (a) electrons and (b) γ-photons at $t = 360$ fs. (c) Angular distribution of γ-photons at laser intensities of $a_0 = 50$, 100, 150, 200, 250, and 300 at $t = 360$ fs. (d) Energy conversion efficiencies of electrons and γ-photons at $t = 360$ fs.

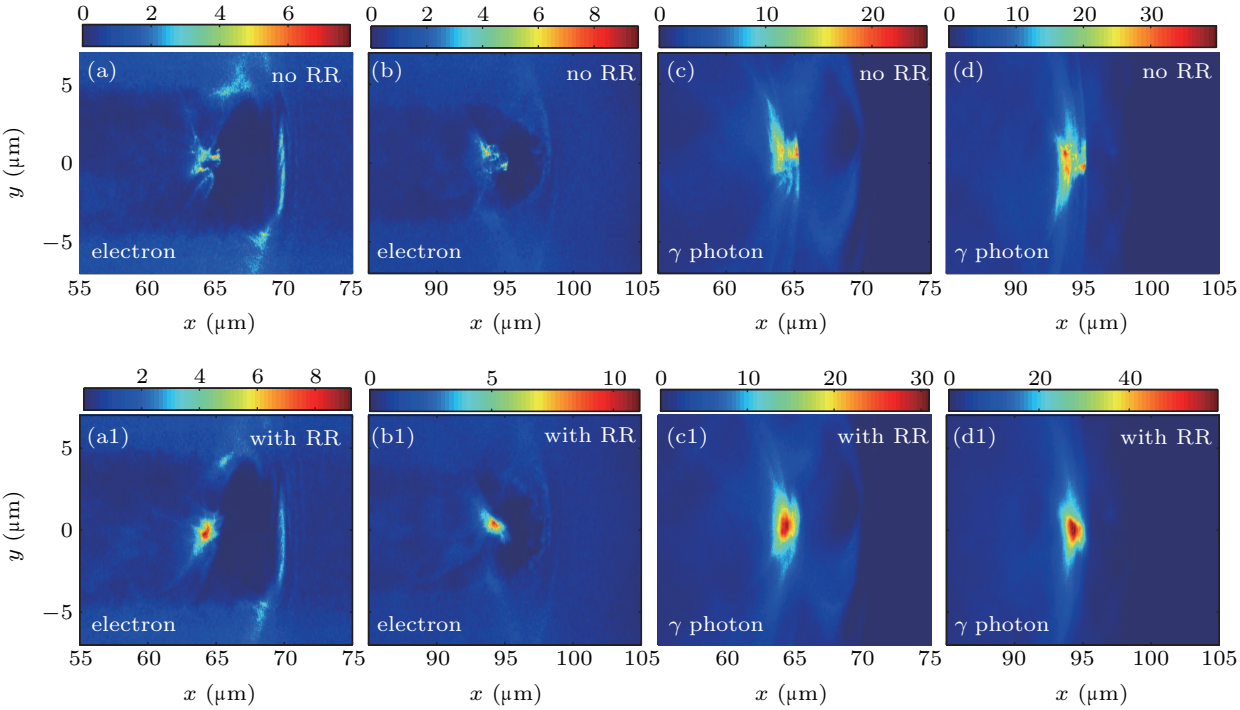


Fig. 11. Distribution of electrons at $t = 250$ fs [(a) and (a1)] and $t = 350$ fs [(b) and (b1)] and of γ-photons at $t = 250$ fs [(c) and (c1)] and $t = 350$ fs [(d) and (d1)] without (top row) and with RR effects for the same laser and target parameters (target 3). Electron and γ-photon densities are normalized by the critical density n_c.

Table 2. The N_e and N_γ are the number of electrons and γ-photons with energy of 1 GeV, E_e and E_γ are the cutoff energies of electrons and γ-photons, η_e and η_γ are the laser energy conversion efficiencies to electrons and γ-photons in the cases of laser intensities from $a_0 = 50$ to $a_0 = 300$ (for LP laser with RR), CP laser (for $a_0 = 250$ and with RR), and without RR (for LP laser and $a_0 = 250$) at $t = 360$ fs for target 3. The channel length and curvature radius are fixed to their optimal values.

Quantity	$a_0 = 50$	$a_0 = 100$	$a_0 = 150$	$a_0 = 200$	$a_0 = 250$	$a_0 = 300$	CP	No RR
N_e (1 GeV)	–	–	1.2×10^{13}	3.5×10^{13}	4.5×10^{13}	5×10^{13}	2.4×10^{13}	1.7×10^{13}
N_γ (1 GeV)	–	–	-	1.2×10^{12}	8.25×10^{13}	3×10^{13}	1.6×10^{12}	3.6×10^{13}
E_e (GeV)	0.2	0.58	1.3	2.3	3.1	3.1	2	4.2
E_γ (GeV)	0.02	0.13	0.5	1.3	2.5	2.6	1.4	3.7
η_e (%)	13	17	23	25	26	27	15	31
η_γ (%)	0.024	0.7	2.8	7	15	26	12	17

6. Summary

An efficient scheme for the generation of ultrabright γ-rays from the interaction of an intense laser pulse with an NCD plasma was studied by using a 2D-PIC simulation. When the intense laser propagates in the NCD plasma, some electrons are trapped in the channel by the self-generated magnetic field and the RR trapping effect and are accelerated to energies of several GeV in the first stage. High-energy, high-density ultrabright γ-photons are emitted by nonlinear Compton scattering as the accelerated electrons collide with the reflected laser pulse in the second stage. The effects of target shape on the generation of bright γ-rays are investigated using three target configurations. Simulation results showed that the presence of a channel and the use of a curved foil target significantly affect the generation of low-divergence, high-energy γ-rays when targets 2 and 3 are used. For target 3, the beam quality of the accelerated electrons is improved, and the density of γ-photons is 4.5 and 1.5 times higher than those for targets 1 and 2, respectively. The peak γ-ray brightness is 4.6×10^{26} photons/s/mm^2/mrad^2/0.1%BW at 100 MeV. Furthermore, the optimal plasma channel length and curvature radius of target 3 for efficient γ-ray emission were also analyzed. The results indicate that the optimal channel length and curvature radius of target 3 are $L = 100$ μm and $r = 6$ μm, respectively. Finally, we investigated the effects of the laser polarization, laser intensity, and RR force on γ-ray emission. A comparison of LP and CP lasers revealed that the laser polarization strongly affects the electron acceleration and the generation of bright γ-rays. With increasing laser intensity, many electrons in the NCD plasma are trapped in the strong laser field region owing to the strong RR trapping effect and form an ultradense electron bunch. As a result, high-density ultrabrilliant GeV γ-rays can be obtained via Compton scattering.

Acknowledgment

The authors are particularly grateful to CFSA at the University of Warwick for allowing us to use the EPOCH code (developed under UK EPSRC Grants (Grant Nos. EP/G054940/1, EP/G055165/1, and EP/G056803/1)).

References

[1] Mourou G A, Tajima T and Bulanov S V 2006 *Rev. Mod. Phys.* **78** 309
[2] Yoon W J, Jeon C, Shin J, Lee K S, Lee W H, Choi W I, Kim T H, Sung H J and Nam H C 2019 *Opt. Express* **27** 20412
[3] Balabanski D L, Popescu R, Stutman D, Tanaka K A, Tesileanu O, Ur C A, Ursescu D and Zamfir N V 2017 *Europhys. Lett.* **117** 28001
[4] Nerush E N, Kostyukov I Y, Fedotov A M, Narozhny N B, Elkina N V and Ruhl H 2011 *Phys. Rev. Lett.* **106** 035001
[5] Liu S Q and Li X Q 2000 *Phys. Plasmas* **7** 3405
[6] Fukuda Y, Akahane Y, Aoyama M, Hayashi Y, Homma T, Inoue N, Kando M, Kanazawa S, Kiriyama H, Kondo S, Kotaki H, Masuda S, Mori M, Yamazaki A, Yamakawa K, Echkina Yu E, Inovenkov N I, Koga J and Bulanov V S 2007 *Phys. Lett. A* **363** 130
[7] Palastro J P and Antonsen T M 2009 *Phys. Rev. E* **80** 016409
[8] Luo W, Liu W Y, Yuan T, Chen M, Yu J Y, Li F Y, Del S D, Ridgers C P and Sheng Z M 2018 *Sci. Rep.* **8** 8400
[9] Piazza A, Muller C, Hatsagortsyan, Karen and Keitel C 2011 *Rev. Mod. Phys.* **84** 1177
[10] Luo W, Wu S D, Liu W Y, Ma Y Y, Li F Y, Yuan T, Yu J Y, Chen M and Sheng Z M 2018 *Plasma Phys. Control. Fusion* **60** 095006
[11] Brown E G, Lee H C, Wijers R A M J, Lee K H, Israelian G and Bethe A H 2000 *New Astronomy* **5** 191
[12] Ruhl H, Bulanov S V, Cowan T E and LisekinaT V 2013 *Plasma Phys. Rep.* **27** 363
[13] Lu Y, Zhang H, Hu Y T, Zhao J, Hu L X, Zou D B, Xu X R, Wang W Q, Liu K and Yu T P 2020 *Plasma Phys. Control. Fusion* **62** 035002
[14] Ma Z G, Yang L H, Liu W Y, Wu S D, Xu Y, Zhu Z C and Luo W 2019 *Matter Radiat. Extremes* **4** 064401
[15] Corde S, Ta Phuoc K, Lambert G, Fitour R, Malka V, Rousse A, Beck A and Lefebvre E 2013 *Rev. Mod. Phys.* **85** 48
[16] Homan D C, Ojha R, Roberts D H and Wardle J F C 1998 *Nature* **395** 457
[17] Rowlands-Rees T P, Kamperidis C, Kneip S, Gonsalves A J, Mangles S P D, Gallacher J G, Brunetti E, Ibbotson T, Murphy C D, Foster P S, Streeter M J V, Budde F, Norreys P A, Jaroszynski D A, Krushelnick K, Najmudin Z and Hooker S M 2008 *Phys. Rev. Lett.* **100** 105005
[18] Hu Y N, Cheng L H, Yao Z W, Zhang X B and Xue J K 2020 *Chin. Phys. B* **29** 084103
[19] Liseykina T V, Borghesi M, Macchi A and Tuveri S 2008 *Plasma Phys. Control. Fusion* **50** 124033
[20] Ferri J and Davoine X 2018 *Phys. Rev. Accel. Beams.* **21** 091302
[21] Zhang G B, Hafz N A M, Ma Y Y, Qian L J, Shao F Q and Sheng Z M 2016 *Chin. Phys. Lett.* **33** 095202
[22] Phuoc T K, Corde S, Thaury C, Malka V, Tafzi A, Goddet J P, Shah R C, Sebban S and Rousse A 2012 *Nat. Photon.* **6** 308
[23] Vargas M, Schumaker W, He Z H, Zhao Z, Behm K, Chvykov V, Hou B, Krushelnick K, Maksimchuk A and Yanovsky V 2014 *Appl. Phys. Lett.* **104** 174103
[24] Matsuoka T, Kneip S, Mcguffey C, Palmer C, Schreiber J, Huntington C, Horovitz Y, Dollar F, Chvykov V and Kalintchenko G 2010 *J. Phys. Conf. Ser.* **244** 042026
[25] Doumy G, Quere F, Gobert O, Perdrix M, Martin Ph, Audebert P, Gauthier J C, Geindre J P and Wittmann T 2004 *Phys. Rev. E* **69** 026402
[26] Boca M and Florescu V 2009 *Phys. Rev. A* **80** 053403
[27] Gong Z, Hu R H, Lu H Y, Yu J Q, Wang D H, Fu E G, Chen C E, He X T and Yan X Q 2018 *Plasma Phys. Control. Fusion* **60** 044004

[28] Luo W, Zhu Y B, Zhuo H B, Ma Y Y, Song Y M, Zhu Z C, Wang X D, Li X H, Turcu I and Chen M 2015 *Phys. Plasmas* **22** 063112
[29] Zhu X L, Chen M, Weng S M, Yu T P, Wang W M, He F, Sheng Z M, Paul M, Jaroszynski D and Zhang J 2020 *Sci. Adv.* **6** 7240
[30] Gu Y J, Klimo O, Bulanov S V and Weber S 2018 *Commun. Phys.* **1** 2399
[31] Bake M A, Tursun A, Aimidula A and Xie B S 2020 *Plasma. Sci. Technol.* **22** 105201
[32] Chang H X, Qiao B, Huang T W, Xu Z, Zhou C T, Gu Y Q, Yan X Q, Zepf M and He X T 2017 *Sci. Rep* **7** 2045
[33] Zhang L Q, Wu S D, Huang H R, Lan H Y, Luo W Y, We Y C, Yang Y, Zhao Z Q, Zhu Z C and Luo W 2021 *Phys. Plasmas* **28** 023110
[34] Böttcher M and Dermer C D 2005 *Astrophys. J.* **634** L81
[35] Ford L H 1984 *Mon. Not. R. Astron. Soc.* **211** 559
[36] Zhao Y, Liu J, Xia G and Bonatto A 2020 *Phys. Plasmas* **27** 073106
[37] Yuan T, Chen M, Yu J Y, Liu W Y, Luo W, Weng S M and Sheng Z M 2017 *Phys. Plasmas* **24** 063104
[38] Zhu X L, Chen M, Yu T P, Weng S M, He F and Sheng Z M 2019 *Matter Radiat. Extremes* **4** 014401
[39] Thomas A, Ridgers C P, Bulanov S S, Griffin B J and Mangles S P D 2012 *Phys. Rev. X* **2** 41004
[40] Landau L and Lifschitz E 1963 *Phys. Today* **16** 72
[41] Jackson J D 1999 *Am. J. Phys.* **67** 841
[42] Duclous R, Kirk J G and Bell A R 2011 *Plasma Phys. Control. Fusion* **53** 015009
[43] Kirk J G, Bell A R and Arka I 2009 *Plasma Phys. Control. Fusion* **51** 085008
[44] Arber T D, Bennett K, Brady C S, Lawrence Douglas A, Ramsay M G, Sircombe N J, Gillies P, Evans R G, Schmitz H, Bell A R and Ridgers C P 2015 *Plasma Phys. Control. Fusion* **57** 113001
[45] Weng S M, Mulser P and Sheng Z M 2012 *Phys. Plasmas* **19** 022705
[46] Weng S M, Murakami M, Mulser P and Sheng Z M 2012 *New J. Phys* **14** 063026
[47] Siminos M, Grech M, Wettervik B S and Fülöp T 2017 *New J. Phys.* **19** 123042
[48] Ji L L, Pukhov A, Kostyukov I Yu, Shen B F and Akli K 2014 *Phys. Rev. Lett.* **112** 145003